Gating of Two-Dimensional Electron Systems in (In,Ga)As/(In,Al)As Heterostructures: The Role of Intrinsic (In,Al)As Deep Donor Defects

Michael Prager, Michaela Trottmann, Jaydean Schmidt, Lucia Ebnet, Dieter Schuh, and Dominique Bougeard*

Institut für Experimentelle und Angewandte Physik, Universität Regensburg, Regensburg D-93040, Germany

(Received 16 September 2021; revised 29 October 2021; accepted 12 November 2021; published 10 December 2021)

We present an analysis of gated (In, Ga)As/(In, Al)As heterostructures, a device platform to realize spin-orbitronic functionalities in semiconductors. The phenomenological model deduced from our magnetotransport experiments allows us to correlate the gate response of the two-dimensional electron systems with the design parameters of the heterostructure, in particular the indium concentration. We explain the occurrence of metastable electrostatic configurations showing reduced capacitive coupling and provide gate-operation strategies to reach classical field-effect control in such heterostructures. Our study highlights the role of the intrinsic (In, Al)As deep donor defects, as they govern the dynamics of the electrostatic response to gate-voltage variations through charge trapping and unintentional tunneling.

DOI: 10.1103/PhysRevApplied.16.064028

I. INTRODUCTION

Quantum wells (QWs) based on (In, Al)As potential barriers have developed into a diverse platform to leverage the spin-orbit interaction for solid-state applications. These QW heterostructures allow engineering and control of the Rashba-type spin-orbit interaction [1–8], opening up prospects [9] for the realization of all-electrical spin transistors [10] and topological superconductivity, including the observation of Majorana zero modes [11–15].

Gating of two-dimensional carrier systems represents a key functionality of these applications and has been frequently used in this context [2–6,16–22]. Interestingly, reports on the microscopic mechanisms of the capacitive coupling between the gates and the two-dimensional systems are scarce, while at the same time similarly designed heterostructures seem to deliver diverse gate responses [16–22], posing the question of the origin of these discrepancies.

Here, we present an extensive experimental study of the gate response of top-gated two-dimensional electron systems (2DESs) confined in (In, Al)As-embedded (In, Ga)As QWs. From our experiments, we deduce a phenomenological microscopic model that allows us to explain and predict the observed features of the gate response. In particular, we elucidate the occurrence of a limited voltage range allowing classical field-effect control of the 2DES, while a broader range leads to a metastable gate response, with limited to vanishing capacitive coupling of the gate to the 2DES. We also demonstrate gate-operation strategies to bring an (In, Al)As-based heterostructure from a metastable situation into the classical field-effect range.

Our model points out the crucial role of intrinsic (In, Al)As defect states in the electrostatics of gated heterostructures, hence highlighting their importance in the design process of (In, Al)As-containing devices for spin-orbitronic applications.

II. EXPERIMENTAL PROCEDURES

Our samples are grown by molecular beam epitaxy (MBE) on a semi-insulating GaAs(100) substrate. The layout of the heterostructures is sketched in Fig. 1(a). Oxide desorption is performed at 620 °C, followed by 100 nm of GaAs and an $Al_{0.5}Ga_{0.5}As$/GaAs ten-period superlattice as lattice-matched smoothing layers. Because of the native lattice mismatch of 7.2% between GaAs and InAs, a $In_xAl_{1-x}As$ step-graded buffer is grown at 335 °C, where $x = 0.1$–0.87 (sample A) in 19 steps or $x = 0.1$–0.82 (sample B) in 17 steps followed by a single step back to $x = 0.81$ (sample A) or to $x = 0.75$ (sample B). Then, the active layers are grown at 440 °C, comprising an $In_xGa_{1-x}As$ QW embedded in 120 nm of $In_xAl_{1-x}As$ below and 130 nm of $In_xAl_{1-x}As$ above. In order to prevent oxidation damage, the structure is completed with a 2-nm $In_xGa_{1-x}As$ barrier. The indium content in the active layers is constant at 81% for sample A and 75% for sample B.

The samples are processed with standard wet etching techniques in a clean-room environment to define a Hall-bar geometry with a width of 20 μm. After etching, Ohmic contacts are realized by deposition of 260 nm of AuGe

*dominique.bougeard@ur.de

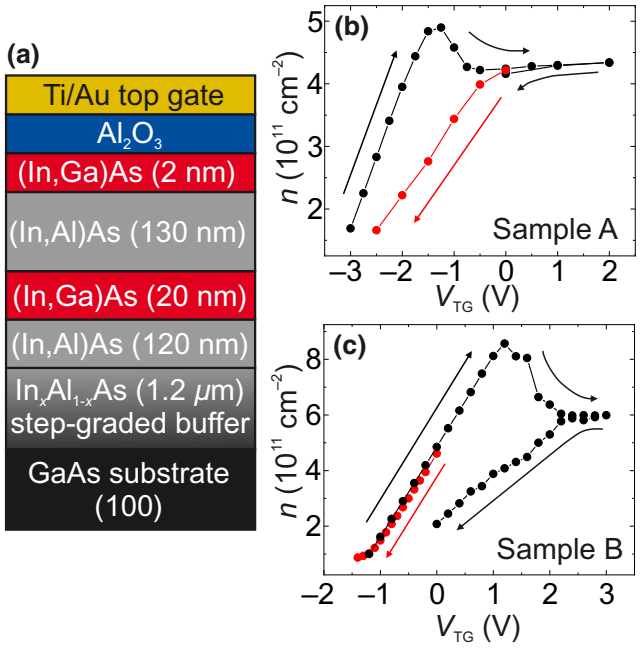

FIG. 1. Gate response of two representative samples A and B. (a) Heterostructure layout. The indium contents are 81% for sample A and 75% for sample B. (b),(c) Electron density n as a function of V_{TG} for sample A (b) and sample B (c). After a cooldown to 4.2 K at $V_{TG} = 0$ V, the system is depleted (red) below the metal-insulator transition, followed by a top-gate upsweep and a subsequent downsweep back to $V_{TG} = 0$ V.

(88%/12%) and 66 nm of Ni, followed by forming-gas-assisted annealing. As a gate dielectric, we deposit 100 nm (sample A) or 50 nm (sample B) of Al_2O_3 via thermal atomic-layer deposition (ALD) at 300 °C, followed by a 10/100-nm Ti/Au top gate (TG).

The measurements, unless otherwise stated, are carried out at a temperature $T = 4.2$ K in a ^{4}He dewar using standard low-frequency lock-in techniques at 17 Hz with an excitation current of 50 nA. Sample A yields a maximum electron mobility $\mu = 506\,000$ cm^2/V s at a density $n = 4.9 \times 10^{11}$ cm^{-2} with a cooldown TG voltage $V_{TG} = 0$ V. Sample B gives $\mu = 258\,000$ cm^2/V s at a density $n = 7.5 \times 10^{11}$ cm^{-2}. In time-resolved measurements of the electron density as a function of the gate voltage, the density is determined by applying a constant magnetic field $B = 500$ mT while sweeping the gate voltage at sweep rates of 1–5 mV/s. For all applied gate voltages, the Hall voltage at zero magnetic field is 0 V. Hence, the linear dependence between the Hall voltage and B gives the density n.

III. RESULTS AND DISCUSSION

A. Gate response

Figure 1(b) displays the gate response, i.e., the electron density n of the 2DES as a function of the TG voltage V_{TG}, for an $In_xGa_{1-x}As$ QW embedded in $In_xAl_{1-x}As$ with $x = 81\%$ (sample A). The gate-voltage cycle applied is the following: The sample is cooled from room temperature (rt) to 4.2 K with $V_{TG} = 0$ V applied, yielding $n = 4.2 \times 10^{11}$ cm^{-2}. The 2DES is then depleted by applying $V_{TG} < 0$ V [red trace in Fig. 1(b)] until the metal-insulator transition (MIT) is reached. The latter occurs below $n = 1.8 \times 10^{11}$ cm^{-2} [last point of the red trace in Fig. 1(b)]. After going to -4 V, V_{TG} is increased: accumulation is then observed from $V_{TG} = -3$ V onwards [black trace in Fig. 1(b)]. A clear hysteresis in the gate response appears, as the black trace differs from the red trace. Both branches exhibit a linear dependence, indicating a classical field-effect response to the gate action. However, the black trace has a steeper slope than the red trace, indicating stronger capacitive coupling of the TG to the 2DES in the QW. When V_{TG} is increased further towards 0 V, the linear part of the black trace ends at a peak density $n_{peak} = 4.9 \times 10^{11}$ cm^{-2}. Then, even when V_{TG} is increased further, meaning that electrons are accumulated in the QW, the measured density quickly decreases, forming a characteristic peak. When V_{TG} is increased even further, this density drop saturates at $n_{sat} = 4.3 \times 10^{11}$ cm^{-2} and does not change significantly up to $V_{TG} = +2$ V. A decrease in V_{TG} again towards $V_{TG} = +1$ V results in no reaction of the 2DES density, indicating a loss of capacitive coupling to the TG between +2 and +1 V. The 2DES reacts again below $V_{TG} = +1$ V: the electron density decreases [black trace in Fig. 1(b)]. Its value at $V_{TG} = 0$ V coincides precisely with the density observed directly after the cooldown [see the merging of the black and the red trace in Fig. 1(b)]. Finally, a decrease in V_{TG} to negative voltages leads exactly to the red trace in Fig. 1(b), closing the hysteresis loop. We observe this hysteresis loop to remain stable when the gate-voltage cycle described is repeated.

Regarding the efficiency of the gate control of the 2DES from the point of view of device applications, two major observations hence emerge from Fig. 1(b): the sample allows significant linear control of the 2DES density with the gate voltage, but this is true in two distinct gate-voltage intervals with two different capacitive couplings (the red and black traces). Furthermore, the maximum electron density that can be reached within these linear regimes is lower for the branch with the smaller capacitive coupling (red trace). The gate controllability can thus be expected to depend strongly on the electrostatic situation before the cooldown, as well as on the gate-sweep history of the sample. While this is rarely commented on in the literature, we find these observations to be experimentally in line with the state of the art: when compared, quite different gating properties are reported for similarly designed heterostructures [16–22], seemingly making a correlation between the gating behavior and the heterostructure layout elusive. Given that most of the previous reports have used heterostructures with 75% indium, and to further illustrate this

point, we show the gate response of sample B in Fig. 1(c): this is a 2DES in a device design that is identical to that of sample A (81% indium), apart from the indium content in the semiconductor heterostructure, which is reduced to 75% here. While this sample B qualitatively yields the same hysteretic elements as does sample A, three striking differences appear: First, when the sample is cooled down from rt at $V_{TG} = 0$ V, the 2DES is now initialized in the steeper linear gate-control regime, while for sample A the regime with the stronger capacitive coupling [black trace in Fig. 1(b)] cannot be accessed when the device is simply cooled down with $V_{TG} = 0$ V applied. Second, driving the 2DES in sample B beyond depletion [red trace in Fig. 1(c)] and then accumulating electrons again (black trace) leaves the 2DES unchanged, as the red and black traces are identical. For sample A, they are not. Finally, and third, the peak electron density $n_{peak} = 8.5 \times 10^{11}$ cm^{-2} and the saturation density $n_{sat} = 6.0 \times 10^{11}$ cm^{-2} are significantly higher in sample B than in sample A.

In the following, we develop a systematic understanding of the observed gating behavior in (In, Ga)As/(In, Al)As heterostructures. Given that the 2DES properties of both samples depend strongly on the gate-sweep history, we start by discussing the reaction to a modification of the rt electrostatics of the samples.

B. Biased cooldown

To modify the electrostatic environment at rt, we apply a certain nonzero V_{TG} at rt and then proceed with a cooldown under the chosen nonzero bias, a procedure termed biased cooldown (BCD) in the following. Figure 2 displays the gate response of the 2DES in sample A after four different biased-cooldown runs in which the gate voltage $V_{TG\,BCD}$ applied at rt is decreased from 0 V to −20 V. The starting point, which corresponds to the chosen $V_{TG\,BCD}$ value, is circled in red for each run. The black curve with $V_{TG\,BCD} = 0$ V is identical to Fig. 1(b) and thus starts in the linear regime with the smaller slope. Applying a negative rt bias $V_{TG\,BCD} = -6$ V (blue trace) results in two important changes: First, after the gate-sweep loop is initialized at $V_{TG\,BCD} = -6$ V, the depletion of the 2DES occurs linearly, but now with an intermediate slope. Second, the maximum electron density is increased compared with the black trace ($V_{TG\,BCD} = 0$ V). The result of reducing $V_{TG\,BCD}$ further, to −15 V (green trace), confirms this trend: now, the first measurement point is located in the linear regime with the steepest slope, and the maximum electron density is further increased. Additionally, the peak, which concludes the steeper-slope regime, is widened. If we go even further, to $V_{TG\,BCD} = -20$ V, the MIT occurs even at rt. When V_{TG} is increased until electron accumulation occurs (at −18.4 V), the system is initialized in the steeper linear branch, as for the green trace. While the maximum electron density does not increase further between

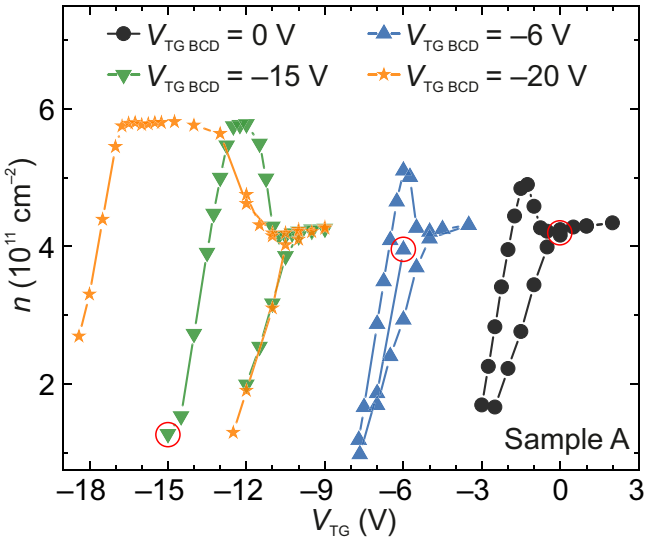

FIG. 2. Electron density n of sample A as a function of V_{TG} for four representative biased-cooldown voltages $V_{TG\,BCD}$. The red circle indicates the first measurement point after cooldown at each $V_{TG\,BCD}$.

the green and the orange trace, the peak, which concludes the steeper-slope regime, is widened into a plateau. From our biased-cooldown studies, which are reproducible across several samples and are shown for sample A as an example here, we draw two conclusions: On a practical level, we demonstrate here, from our very general experimental experience across many samples with different heterostructures, that proper biased cooling allows us to initialize the gated heterostructure into a well-defined state, for example the state with the steepest linear slope. Strikingly, the gate response of the green trace in Fig. 2 very much resembles that for sample B (75% indium and $V_{TG\,BCD} = 0$ V), shown in Fig. 1(c). Thus, the fact that biased cooling of an 81% indium sample allows us to make the gated 2DES behave similarly to a zero-biased 75% indium sample suggests that the gate response of a sample is closely linked to the intrinsic microscopic electrostatics of the heterostructure. Hence, in the following, we discuss and analyze the different parts of the gating cycles presented in Figs. 1 and 2.

C. Charge-transfer model for the gate response

We divide the gate-response hysteresis pattern into characteristic electrostatic regimes, numbered with Roman numerals as presented in Fig. 3. These regimes represent reproducible elements of the hysteresis and do not necessarily coincide with the chronology of the V_{TG} variation after cooling down. The following discussion and the charge-transfer model (CTM) presented are supported by experimental results from many samples with, e.g., different indium contents and different QW depths beyond 50

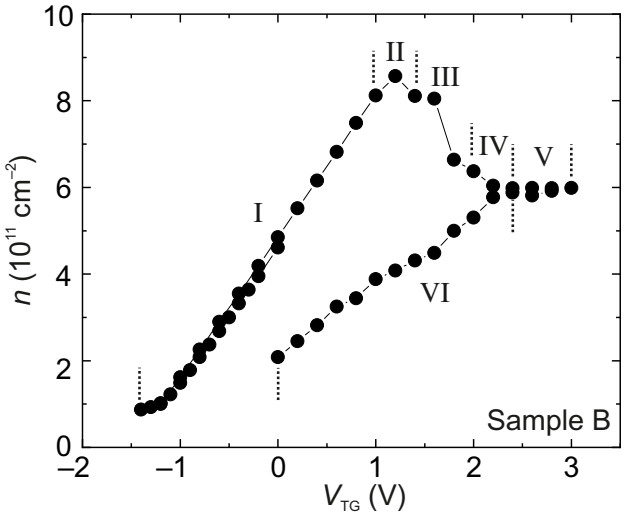

FIG. 3. Electron density n of sample B as a function of V_{TG} at $V_{TG\,BCD} = 0$ V. The different electrostatic regimes, which are discussed in the text, are indicated with Roman numerals.

nm below the heterostructure surface. We use sample B as an example to illustrate our discussion in this section.

1. Regime I

We define the steeper linear segment, which suggests capacitive coupling described by the classical field effect, as regime I. Experimentally, this regime is characterized by two major observations: First, upsweeps and downsweeps of V_{TG} coincide along this branch, and only along this branch: this is not true in the other regimes. Second, when V_{TG} is swept to the next measurement value, the electron density instantly reaches its equilibrium value. This instant reaction is again specific to regime I. As we will see later, in other regimes the experimental determination of the electron density requires settling times for the electron density to reach its equilibrium value after each gate action.

2. Regime II

Regime I has an upper limit, which appears as either a sharp or a more elongated peak (and even transforms into a plateau for $V_{TG\,BCD} = -20$ V in Fig. 2), defined as regime II. Here, even when V_{TG} continues to be increased, the density saturates. This could be a result either of a loss of capacitive coupling between the gate and the 2DES or of a loss of electrons out of the QW. We exclude a loss of capacitive coupling, since the electron density continues to immediately react to a V_{TG} reduction for all voltage values in regime II. While a loss of electrons out of the QW seems counterintuitive at first sight, it becomes more plausible when one looks at the band-edge sketches of the gated heterostructure in Figs. 4(a) and 4(b). These schematic illustrations are inspired by self-consistent Schrödinger-Poisson calculations, for which we use parameters from Refs. [23,24]. Note that, during the MBE growth of (In, Al)As, the formation of intrinsic crystal defect sites in the form of arsenic antisites is inevitable. These arsenic antisites induce two deep-donor-level (DDL) states, which lie 0.12 and 0.17 eV below the conduction-band (CB) edge of (In, Al)As [24]. These act quite effectively as donor states for an (In, Ga)As or InAs QW embedded in (In, Al)As, creating 2DESs with significant electron densities in these QWs through intrinsic doping, even in nominally undoped heterostructures.

Figure 4(a) depicts the CB edge (black lines) for sample B, as well as the evolution of the two energy levels of the DDLs along the growth direction of the heterostructure (dotted colored lines). The electron population is schematically represented by orange dots. Because of the ionization of the DDLs, the evolution of the (In, Al)As CB edge along the growth direction is curved and, in particular, forms a trough shape between the heterostructure surface and the (In, Ga)As QW. In Fig. 4(a), $V_{TG} = 0$ V is applied to sample B, representative of a system initialized in regime I, in a stable configuration, as observed in the experiment. However, when a positive V_{TG} is applied, the band edge bends downwards in the part to the left of the QW in the sketch. From a certain $V_{TG} > 0$ V onwards (the start of regime II), this eventually results in the situation sketched in Fig. 4(b). Compared with Fig. 4(a), this sketch illustrates that electrons in the QW now face an increasingly more transparent triangular-shaped potential barrier between the QW and the DDL states in the (In, Al)As. Simultaneously, the DDL energy is shifted so as to be equal to or even below the lowest subband of the QW. Hence, an increased tunneling probability from the 2DES into the DDLs is expected. These electrons, which are then trapped in the DDLs in the (In, Al)As, do not contribute to the transport anymore and thus appear as lost 2DES electrons in our experiment.

The dynamics shown in Fig. 4(b) is experimentally verified by the measurement depicted in Fig. 4(c). Sample B ($V_{TG\,BCD} = -6$ V) is first set to regime I at $V_{TG} = -4.8$ V, from which we sweep V_{TG} into regime II up to -4.0 V while measuring the electron density of the 2DES over time. Regime I is represented by the instant reaction of the electron density to the classical field effect, i.e., it increases linearly with increasing V_{TG}. At $V_{TG} = -4.6$ V, the density increase then flattens, which we denote as the beginning of regime II. A further increase in V_{TG} leads to a smooth transition into a saturation of the density (even though V_{TG} is increased). As soon as the V_{TG} sweep is stopped within regime II, here at -4.0 V as an example, the density immediately decreases over a duration of several minutes, illustrating the loss of the 2DES electrons. Additionally, Fig. 4(c) shows that the capacitive coupling of the TG to the 2DES in the QW is not lost. At $t = 44$ min, V_{TG} is decreased again, which results in an immediate decrease in

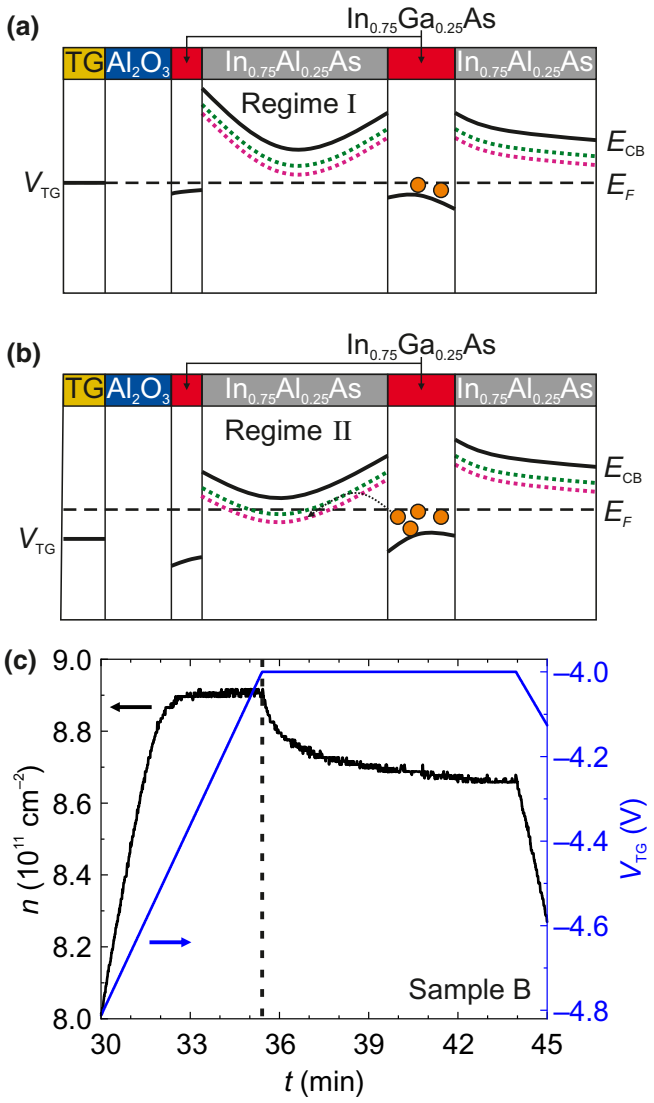

FIG. 4. (a),(b) Conduction-band (CB)-edge sketches of sample B for $V_{TG} = 0$ V (a) and $V_{TG} > 0$ V (b), representative of regime I (a) and regime II (b). The colored dotted lines indicate the energy of the DDLs within the (In, Al)As, lying at 0.12 eV (green) and 0.17 eV (pink) below the (In, Al)As CB edge. The orange dots represent an electron population. With increasing V_{TG}, electron tunneling from the QW into the (In, Al)As deep donor levels sets in. (c) Electron density n (black) of sample B and V_{TG} sweep (blue) at $V_{TG\,BCD} = -6$ V as a function of measurement time t. The sample is initialized in regime I and evolves to regime II at $t = 32$ min.

the density, driven by the classical field effect. This experiment also shows that a settling time on the scale of several minutes is required for the density to reach its equilibrium value after a specific V_{TG} is set. Only in regime I does the measured density not require this settling time. Each density point in the measurements presented in Figs. 1–3 hence includes an appropriate settling time, on the scale of several minutes.

3. Regime III

When a higher V_{TG} is applied at the peak structure of regime II, the band tilting becomes even stronger. Hence, the triangular-shaped potential barrier between the QW and the (In, Al)As becomes even more transparent, effectively further increasing the tunneling rate of electrons from the QW to DDL sites within the (In, Al)As. From our experimental observations, we conclude that the electron tunneling rate becomes significantly larger than the increase in the electron density in the QW induced by the increasing V_{TG} here, thus resulting in a clearly visible loss of electrons. In our model, this steep decrease in the 2DES density characterizes regime III.

Calculating the distance d between two (In, Al)As defect sites of the same type [25] yields $d \approx 32$ nm. The effective Bohr radius of an electron bound to a doping site is calculated as $a_0^* \approx 18$ nm [26]. Comparing these two length scales d and a_0^* suggests field-assisted charge transfer through the (In, Al)As via multistep hopping. This multistep process manifests itself within the experiment, particularly in the comparatively long settling time of the electron density after each adjustment of V_{TG}. At the same time, when V_{TG} is increased, the apex of the trough is shifted towards the interface between the semiconductor and the dielectric. Hence, the increase in V_{TG} facilitates hopping from the trough apex towards this interface, as sketched in Fig. 5(a). In our understanding, when electrons arrive at this interface, they get trapped. Indeed, we have good experimental indications for this picture, shown for example by the gate response in Fig. 5(b): Within a V_{TG} variation in regime I (red trace), no hysteresis occurs, and thus the downsweep to $V_{TG} = -7.5$ V and the following upsweep branch are identical. A reversal of V_{TG} after regime I is left (regimes II and onwards, black curve), on the contrary, results in the opening of a hysteresis, i.e., the branch for the gate-voltage downsweep differs from that for the previous upsweep. The opening of this hysteresis reflects a loss of carriers in the 2DES, which we interpret as a transfer into the interface, where trapping occurs. Our experiments also show that, from regime II onwards, this trapping at the interface is quite stable. Indeed, once an electron is trapped inside the interface, we observe that it cannot be brought back by a large negative V_{TG}. This is depicted in Fig. 5(c): when regime II is reached (in this case in an upsweep to $V_{TG} = -4$ V) and hysteresis occurs, neither a subsequent downsweep to $V_{TG} = -7.5$ V nor a downsweep to $V_{TG} = -9$ V allows us to reset the system back to the initial branch of regime I (red trace). In our experiments, only when the sample is heated up to rt does the system undergo a full reset.

4. Role of the semiconductor-dielectric interface

We believe that the observed stable trapping occurs most plausibly at the interface and results from the complex

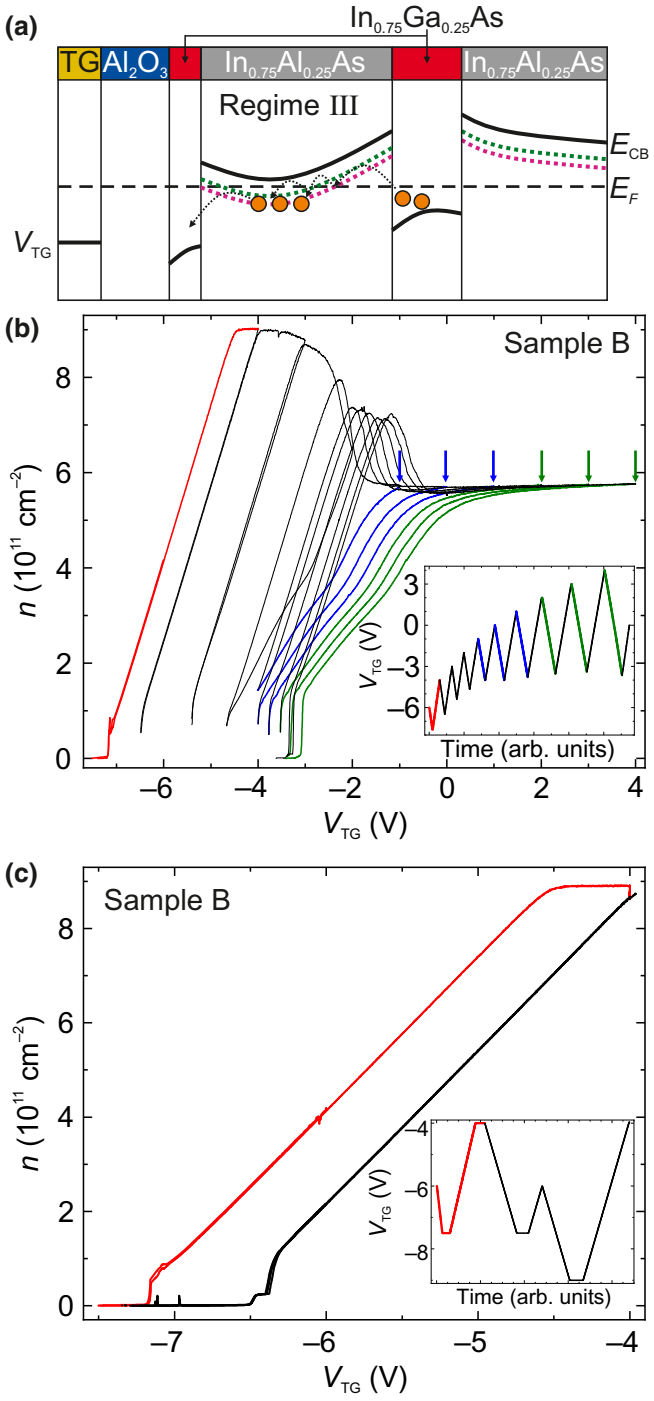

FIG. 5. (a) CB-edge sketch of sample B for increasing V_{TG}, representative of regime III. When V_{TG} is increased, electrons are transferred through the (In, Al)As via multistep hopping tunneling. (b) Electron density n of sample B as a function of V_{TG} at $V_{TG\,BCD} = -6$ V. The red line indicates the starting point of the series. The details of the gate-response series are discussed in the text. The inset depicts the V_{TG} sweeps for the series considered. (c) Electron density n of sample B as a function of V_{TG} at $V_{TG\,BCD} = -6$ V for a 2DES depletion initiated from regime I (red) and from regime II (black). The inset depicts the corresponding V_{TG} sweeps.

morphology of the interface between the semiconductor heterostructure and the dielectric. First, since this interface marks the sharp transition between the single-crystalline semiconductor heterostructure and the amorphous ALD-deposited Al_2O_3 (dielectric), it hosts a significant concentration of point defects, which provide an energetically broad distribution of states [27–33], from shallow defects (which induce instabilities due to trapping and release) to deep defects (which contribute to metastable trapping). Second, it has additionally been shaped by several environmental influences and sample-processing steps—e.g., post-MBE-growth oxidation of the (In, Ga)As cap in air as well as (possibly partial) self-cleaning of the oxidized surface at the beginning of the ALD process [34–41]—creating a spatially inhomogeneous hummocky potential landscape at this interface.

5. Regime IV

In the experiments, the density drop in regime III ends with a smooth transition to a density saturation. The electron density then stays constant when V_{TG} is increased further. This regime is defined as regime IV. Its appearance indicates that when the interface hosts a sufficient threshold population of trapped negative charges, partial screening of the electric field from the TG occurs. This partial screening should induce a flattening of the band-edge profile of the (In, Al)As compared with the unscreened situation, as depicted in Fig. 6(a). As a consequence, the triangular barrier between the QW and the (In, Al)As becomes less transparent again, effectively decreasing the tunneling rate from the QW to the (In, Al)As defect sites. The process that we have just described is self-limiting and thus explains the saturation of the 2DES density: each increase in V_{TG} is directly compensated by an equivalent tunneling-assisted screening.

We have good experimental evidence for the fact that the screening is only partial. To visualize this, one can consider Fig. 5(b) again, which has already allowed us to illustrate the loss of electrons in regimes II and III. We now consider V_{TG} downsweeps that start in regime IV (blue traces, with starting points indicated by blue arrows). For any given V_{TG} value in the range between -1 V and $+1$ V, the density always reacts immediately to a V_{TG} downsweep, as shown by the three blue traces. While the density saturation illustrates the screening, the immediate reaction of the density demonstrates that the screening is only partial.

While throughout the whole of regime IV the system instantly reacts to gate action (although the density saturates), as V_{TG} is increased further, a point occurs from which the access to the 2DES, i.e., the capacitive coupling, is lost. This can be seen in Fig. 5(b), where, when V_{TG} is swept between $+1$ V and $+4$ V (see the three green traces), either in an upsweep or in a downsweep (the downsweeps

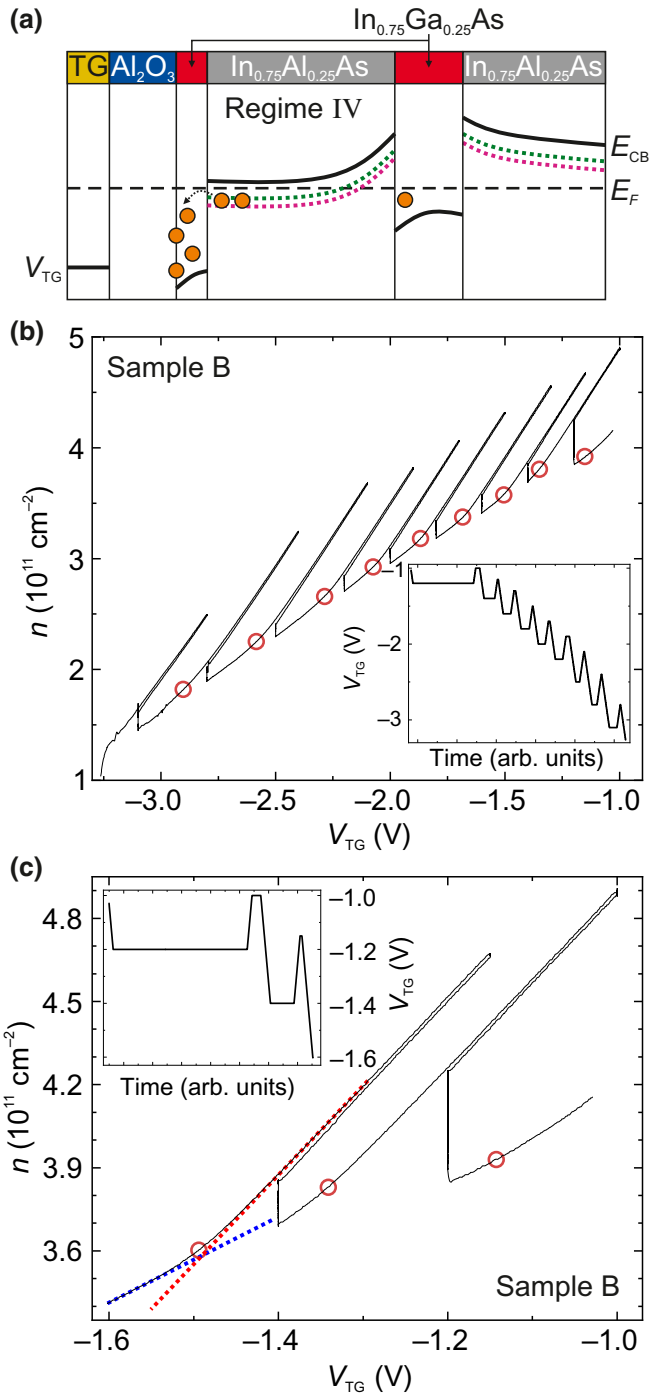

FIG. 6. (a) CB-edge sketch of sample B for increasing (large) V_{TG}, representative of regime IV. The interface between the semiconductor and the dielectric becomes populated. (b) Electron density n of sample B as a function of V_{TG} at $V_{TG\,BCD} = -6$ V within regime VI. The inset shows the V_{TG} sweep routine applied, which is discussed in the text. The red circles indicate the transition point of the two slopes in each TG downsweep branch. (c) Enlargement of (b): the red dotted line indicates the steeper slope value, the blue dotted line the smaller slope value, and the red circles the transition point between these two slope values.

are indicated by green arrows), the density remains constant. This suggests that a regime V exists, here beyond $V_{TG} = +1$ V, in which the capacitive coupling to the 2DES is completely lost.

6. Regime V

In our understanding, this experimental observation translates that when a certain critical trapped electron density at the interface is reached with increasing V_{TG}, the partial screening (regime IV) transitions to full screening (regime V). Hence, the density in the 2DES cannot be adjusted anymore through variation of V_{TG}. This has also been reported for comparable gated heterostructures featuring thicker (10 nm) (In, Ga)As cap layers [22].

Note here one peculiar observation in our experiments: while the charge density trapped at the interface is large enough to fully screen the action of V_{TG}, it does not contribute to the transport data. Even in this regime V, we do not detect any signature of parallel conduction. This is likely due to the previously mentioned hummocky potential landscape that forms at the interface. It seems plausible that such a potential landscape may provide puddlelike minima where charges are trapped locally. These charges can, at best, hop between puddles and hence contribute only negligibly to the experimental transport signatures.

7. Regime VI

Conducting a TG downsweep after going through regimes I–V completes the largest observable gate hysteresis with a branch denoted as regime VI, which we define as the linear regime with a smaller slope in Figs. 1–3. In Fig. 3, the slope of the branch in regime VI is significantly smaller than the slope in regime I. We observe that a settling time of the electron density on the scale of several tens of minutes after a variation of V_{TG} is required, in contrast to regime I; this is similar to the dynamics within regimes II, III, and IV, again indicating substantial charge transfer during regime VI. This motivates a closer look, depicted in Fig. 6(b), where a TG downsweep at $V_{TG} = -1$ V is performed on sample B at $V_{TG\,BCD} = -6$ V. When the TG is swept down to $V_{TG} = -1.2$ V, the density is reduced, revealing the reoccurrence of capacitive coupling after regime V. Stopping at $V_{TG} = -1.2$ V and waiting for a given duration [horizontal line in the inset in Fig. 6(b)], however, reveals a significant increase in the density over several minutes even though V_{TG} is kept constant [indicated by the vertical evolution of the density at $V_{TG} = -1.2$ V in Fig. 6(b)]. Sweeping the TG up after this waiting time reveals a steeper slope for the linear density reaction compared with the slope for the previous downsweep. The density settles instantly in this upsweep, and sweeping down leads to no hysteresis.

This complex behavior in regime VI can be explained as follows: During the downsweep, significant charge transfer counteracts the depletion caused by the TG, resulting in the smaller slope. This charge transfer is a retransfer of electrons that were previously transferred from the QW towards the interface during regimes II–V. During this retransfer, we cannot distinguish where participating electrons had previously been trapped: at the interface or at DDLs. Some of the trapped electrons are irreversibly trapped and cannot be brought back by a large negative V_{TG} [see Fig. 5(c)], and thus they do not contribute to this retransfer in regime VI. As the QW is energetically favorable, these electrons accumulate in the QW, which we see in the measurement as a smaller slope and as a density increase during a waiting time (e.g., at $V_{TG} = -1.2$ V). Since the upsweep that follows a waiting time shows a steeper slope and a downsweep in this branch does not open up a hysteresis, the electron retransfer towards the QW does not operate here. In fact, hysteresis does not appear as long as a certain V_{TG} [red circles in Fig. 6(b)] is not reached in a downsweep. This indicates that the system is in an electrostatic metastable state. Figure 6(c) shows an enlarged part of Fig. 6(b): when V_{TG} reaches a red circle, the slope transitions from a larger [red dotted line in Fig. 6(c)] to a smaller [blue dotted line in Fig. 6(c)] slope value. This switching back to a smaller slope value hence marks the recommencement of electron retransfer into the QW. Notably, the position of the red circles (i.e., the switching back to a smaller slope value) depends on the waiting time before sweeping. This can be seen in Fig. 6(c): the waiting time at $V_{TG} = -1.2$ V (the vertical line in the main graph and the horizontal line in the inset) is significantly larger than that at $V_{TG} = -1.4$ V, resulting in a large ΔV_{TG} between the waiting time at $V_{TG} = -1.2$ V and the red circle ($V_{TG} \approx -1.35$ V) compared with the ΔV_{TG} to the left of the waiting time at $V_{TG} = -1.4$ V. Hence, the abovementioned electrostatic metastable state largely depends on the previous waiting time in this measurement sequence (downsweep, waiting time, upsweep, downsweep). As the nine sequences in Fig. 6(b) illustrate, significant electron retransfer into the QW is present throughout the whole of regime VI until the MIT at $V_{TG} = -3.25$ V is reached. Hence, we show here that regime VI represents an unstable gating region where a depletion of the 2DES is constantly counteracted by electron retransfer from the heterostructure into the 2DES.

D. Temperature dependence

The charge-transfer processes characteristic of regimes II, III, and IV are based on electron tunneling from the QW into the DDLs in the (In, Al)As. Hence, they should be enhanced by thermal assistance. Figure 7(a) thus shows the electron density n of sample B as a function of V_{TG} at $V_{TG\,BCD} = 0$ V for four different temperatures. The sample

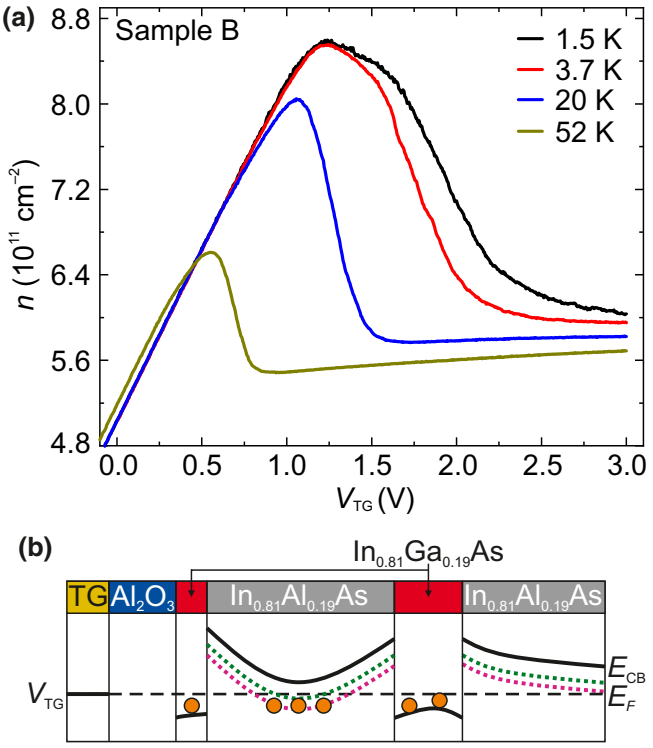

FIG. 7. (a) Electron density n of sample B as a function of V_{TG} at $V_{TG\,BCD} = 0$ V for four temperatures. With increasing thermal energy, the charge-transfer processes are enhanced. (b) CB-edge sketch of sample A (81% indium content) at $V_{TG} = 0$ V, revealing the DDLs to lie below the Fermi energy. This results in a situation similar to regime IV, already visible at $V_{TG} = 0$ V.

is initialized in regime I, and a V_{TG} sweep in the positive direction then covers regimes I to IV. Note that the sample is fully reset at room temperature between each measurement. The observed temperature dependence exactly matches the picture discussed in Sec. III C: the multistep tunneling towards the interface via DDL sites, which marks the transition from regime III to IV, is enhanced by the slightest thermal assistance. This results in a narrowing of the peak (the transition from III to IV) as soon as the temperature is increased, as observed for all four temperatures in our experiment. Also, thermal assistance renders the triangular potential barrier for electrons sufficiently transparent to allow them tunnel into the DDLs at smaller V_{TG}: the transition from regime I to regime II occurs for smaller V_{TG}. Hence, the peak height (at the onset of regime II) is reduced. This is indeed observed with increasing temperature [in particular, the blue and olive-green traces in Fig. 7(a)].

E. Discussion of the indium content

Our experiments and the discussion in the previous sections point out the importance of the intrinsically present DDLs in (In, Al)As in the observed

limitations of the gated operation of (In, Al)As-based heterostructures. Hence, although this has not been addressed in the literature yet, we find that they represent a central parameter in the design of heterostructures for gated operation. For example, given the intrinsic nature of the DDLs, the indium concentration in the (In, Al)As and the depth of the QW below the heterostructure surface will strongly determine the limiting impact of the DDLs on gate operations.

For example, the gate-operation limitations of sample A (81% indium) compared with sample B (75% indium) reported in Fig. 1 can be explained consistently within our model and be tracked down to the DDLs in the (In, Al)As. A band-edge schematic illustration of sample A (81% indium) is depicted in Fig. 7(b) and should be compared with Fig. 4(a) for sample B (75% indium). We assume here that the energy difference between the DDLs (dotted colored lines) and the (In, Al)As CB edge is independent of the indium concentration in the (In, Al)As. However, the band offsets between (In, Al)As, (In, Ga)As, and InAs decrease with increasing indium concentration. As a consequence, for high indium concentrations, tunneling from the QW into the DDLs is enhanced even at $V_{TG} = 0$ V [see Fig. 7(b)], while it is forbidden for lower indium concentrations [see Fig. 4(a)]. Two experimental features reported in our comparison of samples A and B in Fig. 1 result directly from this enhanced tunneling: First, the maximum accessible electron density, as well as the saturation density, is smaller in the sample with the higher indium concentration, sample A. Here, the onset of multistep hopping tunneling from the QW via (In, Al)As DDLs towards the interface (i.e., the onsets of regimes II and IV) requires less gate action compared with a heterostructure with a lower indium concentration. Hence, when the gate operation is started in regime I (see Fig. 1), with similar electron densities, due to this earlier onset of multistep tunneling, the maximum density (reached at the end of regime I) is smaller for sample A (81% indium) than for sample B (75% indium). The same is true for the saturation electron density observed in regimes IV and V (see Fig. 1). Second, for sample A, even at $V_{TG} = 0$ V, the reduced band offsets with increasing indium content induce an electron population in the area of the apex of the trough formed by the DDL energy levels in the schematic illustrations in Fig. 7(b), as indicated by the orange dots. As a consequence, when sample A is cooled down at $V_{TG} = 0$ V, the gated system is initialized in the unstable electrostatic regime VI, as observed in Fig. 1. As explained by our CTM, the device can be brought into the stable regime I only by applying a sufficiently negative V_{TG} to depopulate the DDLs. In contrast, in sample B (with a lower indium concentration), negligible multistep tunneling occurs at $V_{TG} = 0$ V [see Fig. 4(a)], even at rt. Hence, as discussed in Fig. 1, sample B is initialized in the stable gating regime I.

We show in Fig. 2 that sample A may also be initialized in the stable regime I, provided that a negatively biased cooldown is applied (see the green and orange traces in Fig. 2). This is in accordance with our CTM, since, when a sufficiently negative $V_{TG\,BCD}$ is applied at rt, the DDLs are depopulated, as well as the charges trapped at the interface. Then stable gate operation is allowed after a cooldown at this $V_{TG\,BCD}$. Note that, as a direct consequence of this depopulation of charges, this biased cooldown brings the advantage of enabling gate operation up to a higher electron density compared with initialization at $V_{TG} = 0$ V, as seen from a comparison of the orange and green traces with the black one in Fig. 2.

IV. CONCLUSION

In conclusion, our experimental study and charge-transfer model identify that the deep donor levels induced by defects intrinsically present in (In, Al)As play a crucial role in the design process of (In, Ga)As QWs embedded in (In, Al)As for indium contents greater than or equal to 75%, e.g., for spin-orbitronic applications. While providing native *n*-type doping to leverage the strong spin-orbit interaction in 2DESs on the one hand, they substantially determine the electrostatics of the heterostructure through charge trapping and unintentional tunneling events on the other hand. As a consequence, they thus impose limitations that need to be taken into account for top-gated operation of 2DESs in such heterostructures. Strikingly, electrostatically stable gate operation is quite generally possible only in a limited gate-voltage range. A much broader voltage range then displays reduced-to-vanishing capacitive coupling of the gate to the 2DES, induced by unstable or metastable electrostatic configurations, which are governed by charge-transfer processes with long time scales. We show that the design of the heterostructure—most importantly, the indium content—impacts crucially on which electrostatic configuration a sample is initialized in after cooldown. Our model allows us to qualitatively predict how such heterostructures will react to gate operation and how to reach the electrostatically stable regime I. It also explains the observed favorable action of negatively biased cooling to initialize a gated heterostructure in regime I with maximized accessible electron density. Hence, the presence of the deep donor levels should be accounted for in the design of heterostuctures for spin-orbitronics. In particular, trying to maximize the spin-orbit interaction through an increase in the indium content will at the same time minimize the accessible electron density in gate operations.

ACKNOWLEDGMENTS

We acknowledge the financial support of the Deutsche Forschungsgemeinschaft through Project ID 422 31469 5032-SFB1277 (Subproject A01). The authors thank D.

Weiss for access to clean-room facilities and for technical assistance with temperature-dependent measurements.

[1] D. Grundler, Large Rashba Splitting in InAs Quantum Wells due to Electron Wave Function Penetration Into the Barrier Layers, Phys. Rev. Lett. **84**, 6074 (2000).

[2] J. Nitta, T. Akazaki, H. Takayanagi, and T. Enoki, Gate Control of Spin-Orbit Interaction in an Inverted $In_{0.53}Ga_{0.47}As/In_{0.52}Al_{0.48}As$ Heterostructure, Phys. Rev. Lett. **78**, 1335 (1997).

[3] H. Choi, T. Kakegawa, M. Akabori, T. Suzuki, and S. Yamada, Spin–orbit interactions in high In-content InGaAs/InAlAs inverted heterojunctions for Rashba spintronic devices, Phys. E: Low-Dimens. Syst. Nanostruct. **40**, 2823 (2008).

[4] M. Kohda, V. Lechner, Y. Kunihashi, T. Dollinger, P. Olbrich, C. Schönhuber, I. Caspers, V. V. Bel'kov, L. E. Golub, D. Weiss, K. Richter, J. Nitta, and S. D. Ganichev, Gate-controlled persistent spin helix state in (In, Ga)As quantum wells, Phys. Rev. B **86**, 081306(R) (2012).

[5] S. N. Holmes, P. J. Simmonds, H. E. Beere, F. Sfigakis, I. Farrer, D. A. Ritchie, and M. Pepper, Bychkov-Rashba dominated band structure in an $In_{0.75}Ga_{0.25}As$-$In_{0.75}Al_{0.25}As$ device with spin-split carrier densities of $< 10^{11}$ cm^{-2}, J. Phys. Condens. Matter **20**, 472207 (2008).

[6] J. Nitta, T. Bergsten, Y. Kunihashi, and M. Kohda, Electrical manipulation of spins in the Rashba two dimensional electron gas systems, J. Appl. Phys. **105**, 122402 (2009).

[7] P. J. Simmonds, S. N. Holmes, H. E. Beere, I. Farrer, F. Sfigakis, D. A. Ritchie, and M. Pepper, Molecular beam epitaxy of high mobility $In_{0.75}Ga_{0.25}As$ for electron spin transport applications, J. Vac. Sci. Technol., B **27**, 2066 (2009).

[8] Y. Kunihashi, M. Kohda, and J. Nitta, Enhancement of Rashba spin–orbit interaction due to wave function engineering, J. Supercond. Novel Magn. **23**, 49 (2009).

[9] A. Manchon, H. C. Koo, J. Nitta, S. M. Frolov, and R. A. Duine, New perspectives for Rashba spin-orbit coupling, Nat. Mater. **14**, 871 (2015).

[10] P. Chuang, S.-C. Ho, L. W. Smith, F. Sfigakis, M. Pepper, C.-H. Chen, J.-C. Fan, J. P. Griffiths, I. Farrer, H. E. Beere, G. A. C. Jones, D. A. Ritchie, and T.-M. Chen, All-electric all-semiconductor spin field-effect transistors, Nat. Nanotechnol. **10**, 35 (2015).

[11] J. Shabani, M. Kjaergaard, H. J. Suominen, Y. Kim, F. Nichele, K. Pakrouski, T. Stankevic, R. M. Lutchyn, P. Krogstrup, R. Feidenhans'l, S. Kraemer, C. Nayak, M. Troyer, C. M. Marcus, and C. J. Palmstrøm, Two-dimensional epitaxial superconductor-semiconductor heterostructures: A platform for topological superconducting networks, Phys. Rev. B **93**, 155402 (2016).

[12] H. J. Suominen, M. Kjaergaard, A. R. Hamilton, J. Shabani, C. J. Palmstrøm, C. M. Marcus, and F. Nichele, Zero-Energy Modes from Coalescing Andreev States in a Two-Dimensional Semiconductor-Superconductor Hybrid Platform, Phys. Rev. Lett. **119**, 176805 (2017).

[13] J. S. Lee, B. Shojaei, M. Pendharkar, A. P. McFadden, Y. Kim, H. J. Suominen, M. Kjaergaard, F. Nichele, H. Zhang, C. M. Marcus, and C. J. Palmstrøm, Transport studies of Epi-Al/InAs two-dimensional electron gas systems for required building-blocks in topological superconductor networks, Nano Lett. **19**, 3083 (2019).

[14] A. Fornieri, A. M. Whiticar, F. Setiawan, E. Portolés, A. C. C. Drachmann, A. Keselman, S. Gronin, C. Thomas, T. Wang, R. Kallaher, G. C. Gardner, E. Berg, M. J. Manfra, A. Stern, C. M. Marcus, and F. Nichele, Evidence of topological superconductivity in planar Josephson junctions, Nature **569**, 89 (2019).

[15] S. M. Frolov, M. J. Manfra, and J. D. Sau, Topological superconductivity in hybrid devices, Nat. Phys. **16**, 718 (2020).

[16] F. Capotondi, G. Biasiol, D. Ercolani, and L. Sorba, Scattering mechanisms in undoped $In_{0.75}Ga_{0.25}As/In_{0.75}Al_{0.25}As$ two-dimensional electron gases, J. Cryst. Growth **278**, 538 (2005).

[17] C. Chen, I. Farrer, S. N. Holmes, F. Sfigakis, M. P. Fletcher, H. E. Beere, and D. A. Ritchie, Growth variations and scattering mechanisms in metamorphic $In_{0.75}Ga_{0.25}As/In_{0.75}Al_{0.25}As$ quantum wells grown by molecular beam epitaxy, J. Cryst. Growth **425**, 70 (2015).

[18] W. Desrat, F. Giazotto, V. Pellegrini, F. Beltram, F. Capotondi, G. Biasiol, L. Sorba, and D. K. Maude, Magnetotransport in high-g-factor low-density two-dimensional electron systems confined in $In_{0.75}Ga_{0.25}As/In_{0.75}Al_{0.25}As$ quantum wells, Phys. Rev. B **69**, 245324 (2004).

[19] A. T. Hatke, T. Wang, C. Thomas, G. C. Gardner, and M. J. Manfra, Mobility in excess of 10^6 cm^2/Vs in InAs quantum wells grown on lattice mismatched InP substrates, Appl. Phys. Lett. **111**, 142106 (2017).

[20] A. Richter, M. Koch, T. Matsuyama, C. Heyn, and U. Merkt, Transport properties of modulation-doped InAs-inserted-channel $In_{0.75}Al_{0.25}As/In_{0.75}Ga_{0.25}As$ structures grown on GaAs substrates, Appl. Phys. Lett. **77**, 3227 (2000).

[21] J. Shabani, S. Das Sarma, and C. J. Palmstrøm, An apparent metal-insulator transition in high-mobility two-dimensional InAs heterostructures, Phys. Rev. B **90**, 161303(R) (2014).

[22] J. Shabani, A. P. McFadden, B. Shojaei, and C. J. Palmstrøm, Gating of high-mobility InAs metamorphic heterostructures, Appl. Phys. Lett. **105**, 262105 (2014).

[23] I. Vurgaftman, J. R. Meyer, and L. R. Ram-Mohan, Band parameters for III–V compound semiconductors and their alloys, J. Appl. Phys. **89**, 5815 (2001).

[24] F. Capotondi, G. Biasiol, I. Vobornik, L. Sorba, F. Giazotto, A. Cavallini, and B. Fraboni, Two-dimensional electron gas formation in undoped $In_{0.75}Ga_{0.25}As/In_{0.75}Al_{0.25}As$ quantum wells, J. Vac. Sci. Technol. B **22**, 702 (2004).

[25] Defect density $N_D \approx 3 \times 10^{16}$ cm^{-3}, evenly divided between the two types [24,42].

[26] $a_0^* = (\epsilon_{sc}/m^*)(4\pi\epsilon_0\hbar^2/e^2)$, $\epsilon_{sc} = \epsilon_{In_{0.75}Al_{0.25}As} = 13.7$, $m^* = 0.041m_0$ (sc, semiconductor) [43].

[27] M. Choi, A. Janotti, and C. G. van de Walle, Native point defects and dangling bonds in α-Al_2O_3, J. Appl. Phys. **113**, 044501 (2013).

[28] T. Hoshii, S. Lee, R. Suzuki, N. Taoka, M. Yokoyama, H. Yamada, M. Hata, T. Yasuda, M. Takenaka, and S. Takagi, Reduction in interface state density of Al_2O_3/InGaAs

metal-oxide-semiconductor interfaces by InGaAs surface nitridation, J. Appl. Phys. **112**, 073702 (2012).

[29] L. Lin and J. Robertson, Defect states at III–V semiconductor oxide interfaces, Appl. Phys. Lett. **98**, 082903 (2011).

[30] L. Lin and J. Robertson, Passivation of interfacial defects at III–V oxide interfaces, J. Vac. Sci. Technol. B **30**, 04E101 (2012).

[31] J. Robertson, Model of interface states at III–V oxide interfaces, Appl. Phys. Lett. **94**, 152104 (2009).

[32] N. Taoka, M. Yokoyama, S. Hyeon Kim, R. Suzuki, S. Lee, R. Iida, T. Hoshii, W. Jevasuwan, T. Maeda, T. Yasuda, O. Ichikawa, N. Fukuhara, M. Hata, M. Takenaka, and S. Takagi, Impact of Fermi level pinning inside conduction band on electron mobility of $In_xGa_{1-x}As$ MOSFETs and mobility enhancement by pinning modulation, Appl. Phys. Lett. **103**, 143509 (2013).

[33] W. Wang, C. L. Hinkle, E. M. Vogel, K. Cho, and R. M. Wallace, Is interfacial chemistry correlated to gap states for high-k/III–V interfaces?, Microelectron. Eng. **88**, 1061 (2011).

[34] J. Ahn, T. Kent, E. Chagarov, K. Tang, A. C. Kummel, and P. C. McIntyre, Arsenic decapping and pre-atomic layer deposition trimethylaluminum passivation of Al_2O_3/InGaAs(100) interfaces, Appl. Phys. Lett. **103**, 071602 (2013).

[35] C. Hinkle, M. Milojevic, A. Sonnet, H. Kim, J. Kim, E. M. Vogel, and R. M. Wallace, Surface studies of III–V materials: Oxidation control and device implications, ECS Trans. **19**, 387 (2009).

[36] M. L. Huang, Y. C. Chang, C. H. Chang, Y. J. Lee, P. Chang, J. Kwo, T. B. Wu, and M. Hong, Surface passivation of III–V compound semiconductors using atomic-layer-deposition-grown Al_2O_3, Appl. Phys. Lett. **87**, 252104 (2005).

[37] P. C. McIntyre, Y. Oshima, E. Kim, and K. C. Saraswat, Interface studies of ALD-grown metal oxide insulators on Ge and III–V semiconductors, Microelectron. Eng. **86**, 1536 (2009).

[38] M. Milojevic, F. S. Aguirre-Tostado, C. L. Hinkle, H. C. Kim, E. M. Vogel, J. Kim, and R. M. Wallace, Half-cycle atomic layer deposition reaction studies of Al_2O_3 on $In_0.2Ga_0.8As$ (100) surfaces, Appl. Phys. Lett. **93**, 202902 (2008).

[39] M.-S. Park, M. Razaei, K. Barnhart, C. L. Tan, and H. Mohseni, Surface passivation and aging of InGaAs/InP heterojunction phototransistors, J. Appl. Phys. **121**, 233105 (2017).

[40] D. Shahrjerdi, E. Tutuc, and S. K. Banerjee, Impact of surface chemical treatment on capacitance-voltage characteristics of GaAs metal-oxide-semiconductor capacitors with Al_2O_3 gate dielectric, Appl. Phys. Lett. **91**, 063501 (2007).

[41] R. Timm, A. Fian, M. Hjort, C. Thelander, E. Lind, J. N. Andersen, L.-E. Wernersson, and A. Mikkelsen, Reduction of native oxides on InAs by atomic layer deposited Al_2O_3 and HfO_2, Appl. Phys. Lett. **97**, 132904 (2010).

[42] P. N. Brounkov, T. Benyattou, G. Guillot, and S. A. Clark, Admittance spectroscopy of InAlAs/InGaAs single-quantum-well structure with high concentration of electron traps in InAlAs layers, J. Appl. Phys. **77**, 240 (1995).

[43] M. Trottmann, Characterisation of III–V semiconductor hybrid systems for spinorbitronic functionality, Universität Regensburg (2020).